Examining the roles of the easterly wave critical layer and vorticity accretion during the tropical cyclogenesis of Hurricane Sandy

Louis L. Lussier III, * Blake Rutherford, Michael T. Montgomery and Mark A. Boothe

Naval Postgraduate School, Monterey, California

Timothy J. Dunkerton

NorthWest Research Associates, Bellevue, Washington

* *Corresponding author address:* Louis L. Lussier III, 10802 Airport Ct, Broomfield, CO 80021.

E-mail: lussie@ucar.edu

ABSTRACT

We examine the tropical cyclogenesis sequence of Hurricane Sandy and find that genesis occurs within a recirculating Kelvin cat's eye flow of a westward propagating tropical wave. The cat's eye flow is able to provide a protective environment for the mesoscale vortex to grow and is characterized by gradual column moistening and increased areal coverage of deep cumulus convection. These findings are generally consistent with a recently proposed tropical cyclogenesis sequence referred to as the 'marsupial paradigm'.

Sandy's cyclogenesis provides a useful illustration of the marsupial paradigm within a partially open recirculating region, with the opening located south of the pouch center. It is suggested that the opening acts to enhance the genesis process because it is adjacent to an environment characterized by warm, moist air, conditions favorable for tropical cyclogenesis. From a dynamical perspective, we document accretion of low-level cyclonic vorticity filaments into the developing vortex from several sources (the South American Convergence Zone, an easterly wave located west of the pre-Sandy wave, and cyclonic vorticity generated along Hispaniola). Organization and growth of the nascent storm is enhanced by this accretion of cyclonic vorticity. A Lagrangian trajectory analysis is used to assess potential contributions to Sandy's spin-up from a Caribbean Gyre and the easterly wave that formed Hurricane Tony. This analysis indicates that these features are outside of the Lagrangian flow boundaries that define the pre-Sandy wave and do not directly contribute to spin-up of the vortex. Finally, we examine forecasts from the United States and European operational numerical weather prediction models and discuss their effectiveness for this case.

1. Introduction

Hurricane Sandy will be remembered as one of the most devastating storms in US history. Current estimates place the losses in the US alone in excess of $50B (Blake et al. 2013). While much of the focus remains on the recovery effort, the storm itself has provided a fascinating set of questions for hurricane researchers. The objectives of this paper are to answer the following scientific questions: 1) Where did Sandy originate and how did it form? 2) How did features such as the South American Convergence Zone (SACZ), Hurricane Tony, or a Caribbean Gyre impact the tropical cyclogenesis sequence [1]? 3) Are operational numerical weather prediction (NWP) models able to accurately predict Sandy's tropical cyclogenesis?

It will be shown that the first two questions will be answered by drawing upon recent insights of a new tropical cyclogenesis model (Dunkerton et al. 2009) that outlines the dynamics and thermodynamics of the genesis sequence on the synoptic, mesoscale, and convective scales. In this model, the synoptic precursor to genesis is the Kelvin cat's eye formed within the critical layer of a tropical easterly wave (EW)[2]. More precisely, the preferred region of storm formation is located near the intersection of the wave's critical latitude (the locus of points where the background flow equals the phase speed of the parent wave, $u = c_p$) and trough axis (defined as the locus of points with zero meridional wind, $v = 0$). This location

[1] As in Dunkerton et al. (2009), the term cyclogenesis incorporates all of the dynamic and thermodynamic process that lead to declaration of a Tropical Depression by the National Hurricane Center (NHC). For the case of Hurricane Sandy, genesis was declared by NHC at 15 UTC 22 Oct 2012.

[2] For a description of technical terms used in this paper, please refer to the Glossary section of Dunkerton et al. (2009). Additionally, Wang et al. (2010a), their Figure 3, provide a simple schematic documenting the key features of the new tropical cyclogenesis model.

is often referred to as the sweet spot. There are three hypothesized ways (Dunkerton et al. 2009) that the recirculating cat's eye region provides a favorable environment for tropical cyclogenesis: H1) wave breaking or roll-up of the cyclonic vorticity and moisture near the critical surface in the lower troposphere provides the moist vorticity seedlings and a favorable environment for vorticity aggregation; H2) the cat's eye is a region of quasi-closed Lagrangian circulation, and air is repeatedly moistened by convection and protected to some degree from dry air intrusion, which favors a predominantly convective type of heating profile; H3) the parent wave is maintained and possibly enhanced by diabatically amplified mesoscale vortices within the cat's eye. This cyclogenesis sequence is likened to the development of a marsupial infant in its mother's pouch, where the "juvenile" proto-vortex is carried along and protected by the "mother" wave until it is strengthened into a self-sustaining entity. The cat's eye within the wave critical layer is thus dubbed the 'wave's pouch'.

Previous work using observations (Montgomery et al. 2010a, 2012; Rutherford and Montgomery 2012) and numerical simulations (Montgomery et al. 2010b; Wang et al. 2010a,b) have documented the applicability of the marsupial paradigm to the tropical cyclogenesis problem on both the synoptic and mesoscales for EW cases. In this paper, we will test the applicability of the marsupial paradigm using satellite and numerical model analyses for the case of Hurricane Sandy. This study distinguishes itself from previous work by first showing that the parent wave of Hurricane Sandy is weak and thus did not form a completely protected environment (Dunkerton et al. 2009; Wang et al. 2010a). We then demonstrate that cyclogenesis still occurred because the location of the wave pouch opening is adjacent to a favorable external environment, characterized by abundant moisture and cyclonic vorticity.

The third question presented above relates to the ability of operational NWP models

to accurately forecast tropical cyclogenesis. Forecasting tropical cyclogenesis presents a significant challenge because of the multi-scale nature of the process and a lack of in-situ observations. In many cases, to increase lead-time for hurricane warnings, an accurate forecast of genesis is required (as a warning would be necessary prior to the formation of a hurricane). For the past several years, the authors have produced real-time tropical cyclogenesis forecasts based on the dynamical concepts inherent in the marsupial paradigm (Montgomery et al. 2010a; Wang et al. 2009). An assessment of their skill for the case of Hurricane Sandy is presented.

This paper is organized as follows. Section 2 provides information on the data and analysis methods used to examine this case. Section 3 details the genesis sequence of Hurricane Sandy. Section 4 describes the role accretion of vorticity plays in the cyclogenesis and growth of Hurricane Sandy. Section 5 assesses the accuracy of operational NWP tropical cyclogenesis forecasts for the case of Hurricane Sandy. Section 6 presents a summary and discussion of the impacts on our findings to tropical cyclogenesis understanding and points to some of the inherent limitations of operational NWP models.

2. Data and Methodology

As mentioned in the Introduction, the primary source of data used to examine the cyclogenesis sequence of Hurricane Sandy is the operational European Center for Medium-range Weather Forecasts (ECMWF) analyses from 10-22 Oct. These data are available every six hours and have a horizontal grid spacing of 0.25 degrees. Additionally, we use satellite-derived total precipitable water (TPW) from CIMMS to track the pre-Sandy wave. Finally,

we use GOES geostationary satellite data to assess the convective organization prior to formation.

a. Definitions of Lagrangian boundaries

Lagrangian boundaries are impenetrable to advective fluxes, and describe the interaction between nearby flow regions. In contrast to the forthcoming methods that attempt to quantify the contributions of individual flow features, Lagrangian boundaries may be used to exclude the interaction of nearby features that remain separated by a boundary. If the flow was steady, the stable and unstable manifolds of a hyperbolic fixed point form a flow partition as they are not crossed by particles. If the flow is time-dependent, the configuration of the flow boundaries may be quite different. First, the hyperbolic point is not fixed, but is a particle trajectory. A trajectory is called hyperbolic if all solutions of its linearization:

$$\dot{\boldsymbol{\xi}}(\mathbf{x}(t),t) = \nabla\mathbf{u}(\mathbf{x}(t),t)\boldsymbol{\xi} \tag{1}$$

exhibit both exponential growth and decay (Wiggins and Guckenheimer 1992). The stable/unstable manifolds of the hyperbolic trajectory are the sets of solutions that decay to zero forward/backward in time. Algorithms for computing a hyperbolic trajectory and its manifolds are discussed in Ide et al. (2002) and Mancho et al. (2003). The construction of the unstable/stable manifolds requires a choice of a linear segment aligned with the eigenvector of the positive/negative eigenvalue of $\nabla u(x(t),t)$. The manifold is constructed by evolving the initial segment forward/backward in time, and inserting additional points in the manifold as points spread too far apart or in regions with high curvature. For a finite time interval, the unstable manifold is initiated near a hyperbolic fixed point at the begin-

ning of the time interval and advected forward in time. The stable manifold is constructed analogously from the end of the time interval. In time-dependent flows, it is common for the stable and unstable manifolds to intersect at points other than the hyperbolic trajectory. These multiple intersections allow the formation of invariant regions called lobes. Transport through the evolution of lobes, called lobe dynamics (Malhotra and Wiggins 1998), provides a mechanism for particles to be transported across Eulerian streamlines.

In this study, we located persistent hyperbolic stagnation points for the time interval ranging from 00 UTC 18 Oct to 00 UTC 23 Oct. The initial unstable and stable manifold segments were initialized on 18 Oct and 23 Oct respectively. We will show that the stable and unstable manifolds intersect at the hyperbolic trajectories, but also intersect to the north and south of the pouch.

b. Vorticity dynamics

Following Haynes and McIntyre (1987), the flux form of the vertical vorticity equation can be written in pressure coordinates as:

$$\frac{\partial \eta}{\partial t} + \frac{\partial Z_x}{\partial x} + \frac{\partial Z_y}{\partial y} = 0 \tag{2}$$

where η is absolute vorticity defined as: $\eta = \zeta + f$, ζ is the relative vorticity and f is the planetary vorticity. The vector components Z_x and Z_y are defined as:

$$Z_x = u\eta + \omega \frac{\partial v}{\partial p} - F_y \tag{3}$$

$$Z_y = v\eta + \omega \frac{\partial u}{\partial p} + F_x \tag{4}$$

where, u is the zonal component of the wind vector, v is the meridional component of the wind vector, p is the total pressure, ω is the pressure vertical velocity defined as $\omega = \frac{Dp}{Dt}$, and F represents friction and other sub-grid-scale forces per unit mass. By substituting Eq. (3) and Eq. (4) into Eq. (2), the flux form of the vorticity equation can be written in an equivalent vector form:

$$\frac{\partial \eta}{\partial t} = -\nabla \cdot \mathbf{u}\eta - \hat{\mathbf{k}} \cdot \nabla \times \omega \frac{\partial \mathbf{u}}{\partial p} + \hat{\mathbf{k}} \cdot \nabla \times \mathbf{F}. \tag{5}$$

Next we recall Stokes' theorem that the areal integral of absolute vorticity over an area (A) is equal to the absolute circulation around the perimeter of A. Using (5), and applying Stokes' theorem, the vorticity equation (5) may be transformed into the line integral form of the circulation tendency equation:

$$\frac{d\Gamma_a}{dt} = \oint_{\delta A} \eta \mathbf{u} \cdot \mathbf{n} ds - \oint_{\delta A} \omega \frac{\partial \mathbf{u}}{\partial p} \cdot \mathbf{t} ds + \oint_{\delta A} \mathbf{F} \cdot \mathbf{t} ds \tag{6}$$

where Γ_a is the absolute circulation, and $\mathbf{n}$ and $\mathbf{t}$ are the unit normal and tangential vectors, respectively. The first term on the right hand side of Eq. (6) is the 'advective flux' of absolute vorticity and contributes to contributes to the increase or decrease of absolute circulation within the region A due to the horizontal flux (along pressure surfaces) of absolute vorticity across the perimeter of A. The second term is often referred to as the 'tilting-like' term since it shares some similarity with the vortex tilting term in the corresponding material form of the vertical vorticity equation in pressure coordinates (Holton 2004). However, since this term is not proportional to the horizontal velocity, it does not transport horizontally and is termed a 'non-advective' flux term. The third term represents friction and other sub-grid-scale forces and, like the second term, is a non-advective flux term.

The advective flux term will be evaluated to assess the contributions of vorticity accretion to circulation. The advective term will be calculated in boxes centered on and moving with the ECMWF-derived 700 hPa sweet spot position from 0.5-8.0 degree length at 0.5 degree increments. By comparing the magnitude of the contributions of the relative vorticity flux to the planetary vorticity flux, we will attempt to distinguish contributions to the increase in circulation from accretion of vorticity versus that due to positive fluxes of planetary vorticity. The circulation tendency equation, while valid at all times, is somewhat limited in applications using operational global model analyses by the time-resolution of the analysis data. To minimize discretization and sampling errors in these data due to the relatively coarse (6 h) time resolution available to us, we have computed the net flux of vorticity across the periphery of A at each time period of the ECMWF analysis. We then calculated and plotted the average of this net vorticity flux over two successive ECMWF analyses times (e.g., 00 and 06 UTC).

c. Angular momentum fluxes

Absolute angular momentum is defined as:

$$M = v_t r + \frac{1}{2} f r^2 \tag{7}$$

where v_t is the tangential wind, r is the radial distance from the sweet spot, and f is the Coriolis parameter. Spin-up can occur through convergence of M surfaces above the frictional boundary layer where M is approximately materially conserved. In this region, as M surfaces are drawn radially inward, decreasing r leads to an increase in the tangential wind, and indicates a strengthening vortex (Charney and Eliassen 1964; Willoughby 1990).

A related mechanism for spinning up the tangential winds in the boundary layer was recently proposed (Smith et al. 2009; Montgomery and Smith 2014) and will be evaluated for the case of Hurricane Sandy in a forthcoming paper. For the cyclogenesis sequence examined here, we choose to focus on the calculation of Absolute Angular Momentum Fluxes (AMF). It has been suggested (Cheung and Elsberry 2002) that AMF are important in tropical cyclone formation because the radial circulation enhances the cyclogenesis process by "drawing warm, moist air into the center of the developing storm". Additionally, studies have noted (Cheung and Elsberry 2002; Harr et al. 1996) that variations in the magnitude of AMF can be linked to synoptic-scale features. For example, in the development of Typhoon Robyn, it was suggested (Harr et al. 1996) that interaction of the pre-typhoon disturbance with the monsoon trough led to an increase in low-level spin-up through Relative Angular Momentum (RAM) fluxes within 4 degrees latitude radius of the storm. For this study, AMF are calculated (Cheung and Elsberry 2002; Holland 1983) in a cylindrical coordinate system centered on and moving with the ECMWF 700 hPa sweet spot position. If the wind field is decomposed into symmetric and asymmetric components, we can use Eq. (7) to derive an AMF equation (8) and calculate these fluxes across circles of fixed radii:

$$AMF(r) = r\overline{v_r v_t} + r\overline{v_t' v_r'} + \frac{f_o r^2 \overline{v_r}}{2} + \frac{r^2 \overline{f v_r'}}{2} \tag{8}$$

where v_r is the radial wind, f_o is the Coriolis parameter at the center of the disturbance (in this case, the sweet spot), the overbars indicate the azimuthal mean (i.e., the symmetric contribution) and the primes denote eddy contributions, or deviations from this mean (i.e., the asymmetric contributions). The four terms on the right hand side of the equation are: the symmetric RAM flux, the asymmetric RAM flux, the symmetric Coriolis torque, and

the asymmetric Coriolis torque (Cheung and Elsberry 2002).

3. Sandy's tropical cyclogenesis sequence

a. Origin of the pre-Sandy wave

Climatologically speaking, nearly 63% percent of all hurricanes in the Atlantic basin originate from EW precursors (Landsea 1993). This is the case for Hurricane Sandy, as the pre-Sandy wave appears to originate from a breakdown of the Inter-Tropical-Convergence-Zone (ITCZ) on 10 Oct 2012. This reasoning differs from the NHC tropical cyclone report (Blake et al. 2013) that states: "Sandy's origin is primarily associated with a tropical wave that left the west coast of Africa on 11 Oct." Figure 1 is a 4-panel plot of the 700 hPa ECMWF analysis valid at 12-h intervals on 10 and 11 Oct. At 00 UTC 10 Oct (Fig. 1a) the red box outlines the location of the ITCZ as indicated by streamline convergence and an approximately east-west strip of higher relative vorticity values. This time period is the initiation of the ITCZ breakdown as several small-scale waves become evident within the ITCZ. On the western edge of the ITCZ is the disturbance that eventually forms Hurricane Sandy (red arrow). Near 15 W, there is an African easterly Wave (AEW) emerging from the west coast of Africa. Twelve hours later (Fig. 1b), the ITCZ has completely broken down and the pre-Sandy wave is located between 35-40 W, while the AEW is located near 20 W. Over the next 24 h both of these systems propagate westward at speeds of $4 - 5\, m\, s^{-1}$. It is clear in this early analysis that these features are independent disturbances.

We attempted to track the pre-Sandy wave from this point forward. However, the pre-

Sandy wave appears weak over the next several days in the ECMWF analysis and its associated convection is generally minimal as gauged using traditional satellite observations (not shown). Next, we examine the CIMMS TPW product (Fig. 2). On 11 and 12 Oct, the CIMMS TPW product indicates an area of enhances TPW (Fig. 2 a-b, highlighted by the black box) associated with the breakdown of the ITCZ described above. However, from 13-15 Oct (Fig. 2 c-e), there is no clear indication of the pre-Sandy wave as it propagates westward through the area of enhanced TPW located between 30-60 W (centered around 12 N). On 16 Oct, there is evidence of roll-up of the pre-Sandy wave near 55 W (Fig. 2 f). The pre-Sandy wave can be tracked from this point forward in the TPW analysis.

Because the observed moisture signature of the wave is difficult to track, we will use the rotational signature associated with the pre-Sandy wave for tracking between 13-15 Oct. The rotational signature associated with the pre-Sandy wave can be tracked coherently until genesis in a Lagrangian field computed by summing the Okubo-Weiss (OW) parameter along particle paths[3]. The Lagrangian OW field may be defined as $OW_{Lag} = \int \sqrt{OW(x(t))}dt$, where the integrand has the same units as vorticity and is a Galilean invariant quantity. Plotting $\Re(OW_{Lag}) - \Im(OW_{Lag})$ shows the vortex core as maxima, shear sheaths as minimal rings enclosing vortex cores, and Lagrangian manifolds as lines with negative OW_{Lag} values and a sharp gradient of OW_{Lag} normal to the line. If a particle had strain-free vorticity, the OW parameter integrated along the trajectory would show the number of degrees of rotation of that particle measured in radians. For this analysis, we use an integration time of 48 hours

[3]The Okubo-Weiss (Okubo 1970; Weiss 1991) parameter $OW = \zeta^2 - S^2$ is defined herein as the difference between the square of vorticity and total strain, and naturally partitions a flow into rotation-dominated ($OW > 0$) or strain-dominated ($OW < 0$) regions

backward from the present time. The Lagrangian OW field is plotted at the initial location $x(t_0)$. The construction of this field is a time smoothing operation that allows persistent regions of enhanced vorticity to be tracked even in a region with significant flow noise such as the ITCZ. The Lagrangian OW field can be seen in Figure 3 where the pre-Sandy wave is located well south of the larger AEW. Though the Sandy precursor accumulates additional cyclonic vorticity via the accretion process (discussed in Section 4) before becoming a named storm, this region is the primary contributor and initial source of cyclonic relative vorticity within the wave pouch.

To further distinguish the pre-Sandy wave from the AEW, we have examined a Hovmoeller diagram of latitudinally-averaged (10-14 N) TPW from the ECMWF analysis (Fig. a). In this field, we are able to clearly distinguish the pre-Sandy wave from the AEW that leaves Africa on 10 Oct. The disadvantage of this methodology is that it does not indicate the pre-Sandy wave until 11 Oct, as the ITCZ breakdown occurs south of 10 N. Despite this limitation, it seems clear that the pre-Sandy wave originated from a different source than the AEW that moved off the west coast of Africa on 10 Oct.

Due to the complex nature of this case, we have tried many methodologies to identify and track the pre-Sandy wave from inception to genesis. Using a Lagrangian OW field we were able to understand the location of the relative vorticity maximum during the time that the pre-Sandy wave was very weak. Additionally, ECMWF-derived TPW analysis illustrated the independent tracks of the pre-Sandy wave and the AEW that moved off the African coast on 10 Oct. Together, these findings provide compelling evidence that the region of enhanced vorticity originating from the ITCZ breakdown (Fig.1) is the precursor to Hurricane Sandy.

b. Overview of environmental conditions and applicability of the marsupial paradigm

Examining data closer to genesis time, Figure 5 shows the large-scale flow in the Atlantic basin at 18 UTC 19 Oct from the ECMWF analysis. In the earth-relative frame, there is a tropical EW located near 69 W (as indicated by the inverted-V signature of the streamline field); this is the pre-Sandy wave. Over the next several days, the pre-Sandy wave moves westward and a closed cyclonic circulation is not evident in the earth-relative frame until 00 UTC 22 Oct (not shown). Near 52 W, a second EW is the precursor disturbance that becomes Hurricane Tony. There appears to be a filament of cyclonic vorticity that stretches from the pre-Tony wave to the pre-Sandy wave (Fig. 5, top). At this time, the Caribbean basin is rich with areas of cyclonic vorticity that offer the potential for merger with the pre-Sandy wave. Among these enhanced vorticity regions are: i) the SACZ; ii) a weak EW located near 74 W; iii) the island of Hispaniola north of the wave; and iv) a Caribbean Gyre, located directly west of the pre-Sandy wave (81 W). The Caribbean Gyre is a semi-stationary low-level cyclonic circulation evident in the earth-relative ECMWF streamline analysis from 17-21 Oct (Fig. 6).

Figure 6 next illustrates streamlines in the co-moving[4] frame and the evolution of vorticity within the wave pouch. At 18 UTC 19 Oct, the relative vorticity within the wave pouch appears weak and somewhat unorganized. Over the next 72 hours, the system intensifies as the magnitude and areal coverage of positive relative vorticity increases and organizes around the sweet spot. As Sandy begins to organize and intensify, the low-level circulation

[4]A westward phase speed of $-5\,m\,s^{-1}$ was calculated from the latitudinally-averaged (10-14 N) 700 hPa ECMWF analyses meridional wind over the period of 17-22 Oct and is used to produce the co-moving streamline analyses.

associated with the Caribbean Gyre becomes undefined in the co-moving streamline analysis by 00 UTC 21 Oct. There is a remnant filament of cyclonic vorticity on 21 Oct (11 N, 81 W, Fig. 6) located in the same region where the Caribbean Gyre was previously located. However, the origin of this vorticity filament is unclear, as a majority of the cyclonic vorticity associated with the Caribbean Gyre has since advected westward.

One of the salient characteristics of the flow evident in the co-moving streamline analysis is that moist air from the south has a pathway to come very close to the southern periphery of the recirculating region (Fig. 6), an idea examined further in Section 4. On the large-scale, the region of the Caribbean that the pre-Sandy wave is entering is more moist than much of the Atlantic basin (Fig. 5, bottom). The flow orientation around the Caribbean Gyre and the convection associated with it likely contributed to moistening the western Caribbean at this time. In the co-moving frame (Fig. 6, right): i) the wave pouch is more moist than the surrounding environment; and ii) the amount of moisture within the wave pouch increases over time. By 22 Oct, the values of specific humidity on the 850 hPa pressure surface have increased to over $12\,g\,kg^{-1}$ within the entire wave pouch, with maximum values centered on and to the southwest of the sweet spot position. The two mechanisms responsible for this increased moisture are the advection of moist air through the opening in the wave pouch to the south (discussed further Section 4) and continuous moistening by increased convection over time.

Figure 7 is a six-panel plot of six-hour mean infrared (IR) brightness temperatures from the 10.7 μm channel of the GOES geostationary satellites overlaid with 850 hPa streamlines in the co-moving frame from the ECMWF analysis. There is a low-level cyclonic circulation and a recirculating region evident late on 17 Oct (near 59 W and 13 N) as the disturbance

reaches the Lesser Antilles Islands. At this time, convective activity, as depicted here by the cold cloud-top temperature, is minimal within the recirculating region. The circulation weakens somewhat early on 18 Oct (not shown) and becomes elongated southeast to northwest temporarily until re-consolidating as convective activity returns near the center (and to the southeast) by 18 UTC. Subsequently, a low-level circulation persists afterwards as the disturbance moves slowly westward. The growth in horizontal size of the cyclonic circulation at 850 hPa seems most pronounced between 20 and 21 Oct[5]. While convective activity tends to become more focused around the sweet spot (i.e., the center of the cyclonic circulation) with time, the convective maximum is not centered on the sweet spot position, or co-located with the vorticity maximum. Asymmetries in the convection, especially on 20-21 Oct tend to occur in the region east of center where the abundant moisture to the southeast is entrained into the storm and stronger north through northwesterly wind shear is present (not shown).

Finally, the evolution of vertical wind shear as depicted in the ECMWF analysis (Fig. 8) indicates that the pre-Sandy disturbance is moving into a more favorable environment

[5]The scales of the pouch are determined initially by the easterly wave roll up process around the critical level in the lower troposphere (below the 600 hPa level). This is generally a nonlinear process and there is not a precise scaling factor for all circumstances as far as we are aware. Linear theory predicts that the characteristic meridional scale for the critical level is given by the ratio of the meridional shear of the zonal mean wind to the ambient meridional potential vorticity gradient. However, nonlinear processes soon dominate the dynamics (after the absorption phase) and the meridional scale is modified from this first-guess (linear) scaling to one depending on the wave's initial amplitude, the meridional shear of the mean flow at the critical level and the nonlinear wave's "bounce frequency" (Killworth and McIntyre (1985); Schecter and Montgomery (2006), Section 5 and references therein). The longitudinal scale is generally a fraction of the wavelength of the easterly jet flow.

for formation. On 17 Oct, the 850-200 hPa shear over the wave pouch (as calculated in a 3° x 3° box centered on and moving with the sweet spot position) is greater than $20\,m\,s^{-1}$. As the wave moves into the Caribbean basin on 19 Oct, the deep layer shear decreases to $4-9\,m\,s^{-1}$ in the vicinity of the storm, and remains at these lower values until genesis time.

In summary, the foregoing analysis has established that the environmental conditions in the pre-Sandy region are generally favorable for cyclogenesis and that aspects of the marsupial paradigm are evident in Sandy's tropical cyclogenesis sequence. Next, we will evaluate the evolution of the flow boundaries and illustrate the role of vorticity accretion in the tropical cyclogenesis sequence.

4. The role of vorticity accretion in the tropical cyclogenesis and growth of Hurricane Sandy

a. First-order contributors: SACZ and weak EW

The closure of the northern boundary and permeability of the southern boundary surrounding the pre-Sandy circulation center can be seen by examining the Lagrangian boundaries that account for the time-dependent flow field. Here, the Lagrangian boundaries are the stable and unstable manifolds of a pair of hyperbolic trajectories, one to the east of the pouch and another to the west of the pouch. The manifolds form a complete boundary on the north side of the pouch that includes some air from north of the pouch center on 19 Oct (Fig. 9). By 20 Oct, the northern manifolds have moved to within 3 degrees of the circulation center. For the entire period beginning on 19 Oct, there is an open pathway

from the south of the pouch. A trajectory analysis through the construction of tracer fields provides further detail about transport into the pouch. As is normally the case, the tracer gradients align with the true Lagrangian boundaries in the flow, and much of the horizontal transport across the pouch boundaries can be described by regions of accumulation of high or low tracer values (Rutherford and Montgomery 2012). A 'latitude tracer' field at the 850 hPa surface (latitude advected forward for 48 hours and assuming no sources or sinks) can be seen in Figure 9 for the Sandy disturbance at 850 hPa from 19 Oct to 22 Oct at the 00 UTC analysis time. The latitude tracer fields and the shape of the manifold segments from 19-22 Oct show the overturning signature of a breaking wave.

As the disturbance translates westward and evolves from 18-20 Oct, it approaches a region in the Caribbean Sea with θ_e values on the 850 hPa surface that are above 345 K (not shown). These values represent a favorable thermodynamic environment for deep convection and vorticity amplification by vortex-tube stretching in the low and middle troposphere (Kilroy and Smith 2012). The open pathway from the south allows the very moist air from the south and southeast to become entrained into the pre-Sandy wave while excluding the drier air to the north. The latitude tracer field from 21 Oct (Fig. 9) onward confirms that most of the air at the center of the disturbance originated from the moist region at lower latitudes, while any of the air from higher latitudes was initially located within the unstable manifold (blue). The Lagrangian manifolds at other vertical levels indicate that a coherent wave pouch exists up to 500 hPa by 00 UTC 20 Oct. At the 500 hPa level (not shown) the Lagrangian boundaries are in similar locations as those at lower-levels, with a boundary north of the pouch center that acts to prevent dry air from entering the disturbance, and an opening in the boundary to the south. As is the case at lower levels, there is a substantial

stream of moisture from South America evident at the 500 hPa level that is entrained into the core of pre-Sandy wave along the east side of the inner pouch. This moistening of the wave pouch is aided further by the convective moistening over the central Caribbean (Fig. 6). The vertical coherence of the pouch boundaries may help to explain both the size and resilience of Sandy.

Having established the presence of an open boundary to the south of the wave pouch, we will next examine the vorticity transport into the wave pouch. Figure 10 is a six-panel plot of relative vorticity and co-moving streamlines at 12-hour intervals for 20-22 Oct. Focusing first on the SACZ, the beginning of vorticity accretion into the wave pouch occurs on 20 Oct (Fig. 10, A). By 12 UTC, 21 Oct, there is a large area of cyclonic vorticity generated within the SACZ that is attracted to the vortex center. Large areas of cyclonic vorticity continue to be aggregated into the developing vortex through the opening of the cat's eye circulation south of the sweet spot through genesis time (Fig. 10, A). This region provides the most substantial transport of cyclonic vorticity into the pouch and is allowed by the reconfiguration of the boundary to the south and southeast. As discussed above, as the manifolds evolve, the boundary to the north of the pouch remains largely unchanged, and no significant transport occurs there.

We now discuss the boundary between the weak EW and the Sandy critical layer through this evolutionary time sequence. A portion of the cyclonic vorticity from the weak EW (Fig. 10, B) is able to ultimately merge with the vorticity in Sandy's core. This is borne out in the Lagrangian manifolds where, to the west of the circulation center, the lobe dynamics mechanism allows some vorticity from the weak wave to enter the circulation (Fig. 11). The lobe is most easily identifiable on 20 Oct (Fig. 11a), where it is located near 16N, 73W. By

21 Oct, there is no distinction between vorticity from the EW and the building vortex (Fig. 10).

To quantify the contributions of accretion of vorticity, we examine terms from the circulation tendency equation (Eq. 6). Figure 12 is a three-panel plot of the 850 hPa ECMWF derived six-hour averaged advective flux of absolute (black), relative (red), and planetary (green) vorticity at 00 UTC 20-22 Oct. On 20 Oct (Fig. 12a), the magnitudes of the relative and planetary vorticity fluxes within the 4.5 degree length box are nearly equal. Outside of this region, positive contributions to increased circulation are dominated by the flux of planetary vorticity. Azimuthally-averaged profiles of tangential wind from the 850 hPa ECMWF analysis at 06 UTC 20 Oct (Fig. 13), indicate a broad region of higher tangential wind within a 2.25 degree radius of the sweet spot position and a decrease in the tangential wind speed in radii beyond that location. On 21 Oct, there is positive advective flux of absolute vorticity dominated by the relative vorticity flux term beyond two degrees. This region broadly coincides with a large area of higher tangential wind in the ECMWF profile six hours later (Fig. 13). On 22 Oct, there is a maximum in the contribution of relative vorticity flux between 4.5-6 degrees length (Fig. 12c). Beyond this distance, planetary vorticity fluxes dominate contributions to the absolute advective flux. The tangential wind profile on 22 Oct (Fig. 13) illustrates a broadening of the maximum wind region that coincides with these increased absolute vorticity fluxes.

While only the 00 UTC circulation tendency plots are shown here, the other time periods indicate similar results (the 18 UTC plots indicate the largest amounts of spin-up from relative vorticity fluxes, and is suggestive of the maximum time of vorticity accretion). Overall, these data indicate that: i) fluxes of relative and planetary vorticity both contribute

to spin-up of the tangential wind with neither term appearing to be consistently dominant. ii) The contributions of relative and planetary vorticity fluxes vary with time and distance from the sweet spot position, and no clear trend emerges as genesis nears. This is likely attributed to a number of factors including the horizontal and temporal resolution of the ECMWF analysis, the diurnal cycle (e.g., Gray and Jacobson Jr. 1977) and chaotic nature of convection, and the intermittent nature of the accretion process.

From the foregoing analysis, we can draw some important conclusions on the role of vorticity accretion in vortex intensification and growth. First, there are several instances where the relative vorticity flux is the major contributor to the advective flux of absolute vorticity. These regions are at distances that coincide with the previously identified locations of vorticity accretion into the wave pouch (Fig. 10). Second, the broadening and increasing magnitude of the low-level tangential wind profiles over time coincide fairly well with the maxima in the advective flux of absolute vorticity. Given that several of these areas are dominated by the advective flux of relative vorticity associated with accretion, it appears that the accretion process acts to intensify and broaden the vortex during the tropical cyclogenesis stage in the case of Hurricane Sandy.

b. Second-order and non-contributors: Hispaniola, pre-Tony, and the Caribbean Gyre

The contributions to Sandy's genesis from the vorticity generated along Hispaniola, within the Caribbean Gyre, and from the pre-Tony wave are less clear. Our analysis of the Lagrangian boundaries indicates that accretion of cyclonic vorticity from the southern coast of Hispaniola (Fig. 11) likely occurred early in the cyclogenesis sequence when the

stable manifold was elongated northward. These contributions are short-lived and likely small in magnitude. The strongest vorticity filaments generated along the northern portion of Hispaniola and Cuba are not entrained into the pouch during the cyclogenesis sequence as they are outside the northern Lagrangian boundary. The small amount of cyclonic vorticity located near 11 N, 81 W on 18 UTC 21 Oct (Fig. 10, D) is initially located within the stable manifold and thus is able to merge with the outer region of the developing Sandy vortex. This remnant vorticity is transported around the southern periphery of the wave pouch and is aggregated on the periphery of the growing vortex on 22 Oct (Fig. 10). The contributions from this feature to spin-up are likely minimal and mostly impact growth of the outer vortex late in the cyclogenesis sequence. Cyclonic vorticity associated with the Caribbean Gyre is initially located outside of the Lagrangian boundary that defines the western edge of the wave pouch (Fig. 11) and has no pathway to enter the wave pouch prior to genesis. Finally, the pre-Tony wave lies outside of the Lagrangian boundaries of the pre-Sandy wave and there is almost no contribution to the circulation tendency [6].

Potential contributions of the pre-Tony wave and the Caribbean Gyre are quantified further using low-level AMF analysis, as foreshadowed in Section 2. Figure 14 is a 5-panel Hovmoeller diagram of each term from the AMF equation (Eq. 8) calculated within 100 km radius circles centered on and moving with the sweet spot center. Negative values of AMF

[6]In addition to these features, influences of Hurricane Rafael on the pre-Sandy wave were examined thoroughly in our research. Although Hurricane Rafael acted to alter the low-level flow in the central Atlantic from 17-18 Oct and possibly the steering flow of the pre-Sandy wave, we have shown that it had no effect on the transport of vorticity into the Sandy disturbance. For this reason a more in-depth discussion of potential influences of Hurricane Rafael on the pre-Sandy wave was omitted from the paper.

indicate inward transport of absolute angular momentum and implicate a positive tendency to amplify the mean tangential wind field around the circulation center. The dominant terms, especially at larger radii, are the symmetric and asymmetric Coriolis torques. The dominance of these terms at these radii is to be expected, as these terms are proportional to r^2, whereas the RAM flux terms are proportional to r.

The contributions to the pre-Sandy disturbance from the pre-Tony wave and the Caribbean Gyre are evident in the Asymmetric RAM Flux term. The distance between the pre-Sandy disturbance and the center of the pre-Tony disturbance is indicated at each time period by the filled circles (Fig. 14). Contributions from Hurricane Tony to Hurricane Sandy's spin-up are either negligible (when compared to the magnitude of the Coriolis terms) or are opposing spin-up (after 20 Oct) of the pre-Sandy disturbance [7]. Any potential contributions from the Caribbean Gyre (Fig. 14, triangles) are much smaller than those of the Coriolis terms. These data, combined with the fact that the Caribbean Gyre is shown to be completely excluded from the pre-Sandy wave pouch (as it lies on the opposite side of an unstable manifold boundary) suggests that any direct contributions to spin-up from the Caribbean Gyre are negligible or non-existent.

[7]The AMF displayed are presented as an azimuthal average about the sweet spot of the pre-Sandy disturbance. Consequently, Tony is not the only feature contributing to the Asymmetric RAM at this radius. However, in examining the ECMWF data, there do not appear to be any features at similar radii to Hurricane Tony that would provide large enough positive contributions to the Asymmetric RAM fluxes to counteract potentially stronger negative Asymmetric RAM flux from Hurricane Tony.

5. Accuracy of real-time forecasts

For the past five years, the Montgomery Research Group has produced real-time tropical cyclogenesis forecasts (Wang et al. 2009) using operational NWP models (forecasts available at: http://met.nps.edu/ mtmontgo/index.html). The forecast process begins with the subjective identification of a precursor disturbance using satellite, global analysis, and NWP data. Forecasts are then produced out to five days using output from five global weather prediction models. This methodology, based on the ideas of the marsupial paradigm summarized in the Introduction, is predicated on the assumption that the model analysis is able to accurately represent the precursor disturbance on the synoptic-scale.

An assessment of the accuracy of these tropical cyclogenesis forecasts for the case of Hurricane Sandy is presented. Figure 15 is a 4-panel plot of 5-day forecast positions (left) and intensity (right) for the ECMWF (top) and the National Center for Environmental Prediction's Global Forecast System (GFS) (bottom) forecast models. Position error in these forecasts is defined as the difference between the 700 hPa model sweet spot forecast position and the NHC position at the time of tropical depression declaration (15 UTC 22 Oct). The ECMWF and GFS are both able to resolve the pre-Sandy wave in the earth-relative frame at the initial time of each of these model forecasts.

Based on the indicated position errors (Fig. 15, left), the spread of the GFS predicted location at genesis time is smaller than the ECMWF forecasts. The average position error derived from the 00 UTC forecast over five days are 191 km for the GFS and 247 km for the ECMWF. The ECMWF position error decreases substantially by the 22 Oct forecasts and becomes superior to the GFS forecast position. For the intensity forecasts (as measured by

average relative vorticity within a 3°x3° box, centered on and moving with the sweet spot position), both models are similar on 18 Oct (no indication of development) and 21 and 22 Oct (indicating development). Both forecast models indicate a period of intensification followed by a leveling off of the vorticity values on 19 Oct (although the ECMWF indicates a stronger vortex). The ECMWF and GFS both indicate a general trend of increasing vorticity on 19 Oct and in the 12 UTC 20 Oct forecast. There appears to be a more consistent intensification of the vortex in the ECMWF as the forecast initial time becomes closer to genesis.

Although Shen et al. (2013) use idealized numerical simulations to illustrate that the genesis of Hurricane Sandy can be predicted out to 136 hrs, we can only say with certainty that the *operational* deterministic model forecasts indicate development at 00 UTC 21 Oct. The forecasts of Hurricane Sandy using the marsupial techniques were somewhat unique in that the parent wave which supported development of the storm was very weak, a situation not encountered often in the past several years of our real-time forecasts. While there were limits to predictability in the case of Hurricane Sandy, it is encouraging that the operational global forecast models performed fairly well, despite the weak initial structure of the pre-Sandy wave.

6. Discussion and Conclusions

In this paper we examined the tropical cyclogenesis sequence of Hurricane Sandy within the framework of the marsupial paradigm. We show that the origin of Hurricane Sandy was an easterly wave that formed from a breakdown of the ITCZ in the eastern Atlantic Ocean

on 10 Oct. The pre-Sandy wave could be tracked as a coherent (albeit weak) vortex from this time to the beginning of its intensification in the eastern Caribbean Sea. The Caribbean Sea provided a thermodynamic and dynamically favorable environment for cyclogenesis as it was characterized by abundant moisture and numerous filaments of cyclonic vorticity.

The presence of these cyclonic vorticity filaments result in a cyclogenesis process that is a scientifically interesting illustration of the basic marsupial model of tropical cyclogenesis in conjunction with vorticity accretion processes from the perimeter of the wave-pouch region. Lagrangian manifolds indicate that the southern boundary of the Kelvin cat's eye circulation is in fact open, an idea originally suggested in Dunkerton et al. (2009). While the opening of a wave pouch can be detrimental to cyclogenesis if dry air enters into the opening (Rutherford and Montgomery 2012; Riemer and Montgomery 2011), in the case of Hurricane Sandy the opening appears to contribute to genesis due to its fortuitous juxtaposition with a favorable thermodynamic environment and seedling vorticity anomalies. Upon entering the eastern Caribbean basin, the wave pouch was presented with several opportunities to grow via accretion with various strands of cyclonic vorticity from the SACZ, a weak EW to the west, and the island of Hispaniola.

By examining Lagrangian boundaries and the evolution of the vorticity field we are able to fully describe the process of vorticity accretion as it pertains to Sandy's tropical

cyclogenesis. In the accretion process, the sweet spot appears to act as an attractor [8] to multiple areas of cyclonic vorticity located in the Caribbean basin. First, we identify an opening in the Lagrangian boundary south of the vortex center that allows cyclonic vorticity from the SACZ to continuously enter the wave pouch during the cyclogenesis sequence. Second, cyclonic vorticity from a weak EW located west of the pre-Sandy wave is able to merge with and grow the initial vortex through the lobe dynamics mechanism. These two features (along with the initial vorticity associated with the pre-Sandy wave) appear to be the first-order contributors to the intensification and growth of the pre-Sandy vortex during the cyclogenesis sequence. Vorticity accretion from Hispaniola plays a secondary role in Sandy's genesis when compared to contributions from the SACZ and the weak EW. While the Caribbean Gyre and the pre-Tony wave may have played a role in preconditioning the environment prior to genesis, our analysis indicates that these features do not contribute to vorticity accretion during Sandy's tropical cyclogenesis sequence. Additional vorticity accretion occurs post-genesis as the system moves north of Cuba, contributing to the extreme growth of the system. These conditions will be examined in a forthcoming paper.

In summary, the growth of the vortex appears to occur in two stages as higher values of cyclonic relative vorticity are pulled into the wave pouch, followed by a spatial expansion of the pouch as it moves northward. These findings indicate that the formation of Sandy

[8]Our definition of the term "attractor" is not strictly tied to that found in the AMS glossary. Our definition can be inferred from how we used the term in Dunkerton et al. (2009), Montgomery et al. (2010b), Wang et al. (2010), and Montgomery et al. (2012). Broadly speaking, it denotes the tendency of the convective activity and/or cyclonic vorticity to become progressively focused around the sweet spot of the parent easterly wave during the formation of the tropical depression vortex.

was predicated on circular organization resulting from the intricate entrainment of multiple vorticity filaments, and was assisted by numerous episodes of vigorous deep convection in the developing proto-vortex over the warm waters of the central Caribbean basin.

Sandy's pathway to genesis was difficult to anticipate because the pre-Sandy wave was weak by all traditional metrics, and is thus expected to have limited predictability. To put the current findings in perspective, our scientific analyses of the genesis of Atlantic Hurricane Nadine in 2012 (sampled by NASA's Hurricane Sentinel 3, NASA (2013)), exhibited a coherent large-scale synoptic feature over seven days in advance of genesis time. For the case of Hurricane Sandy, the formation of a coherent precursor can be regarded as a complex chain of smaller-scale events. The findings herein suggest that some genesis events are better resolved in large-scale analyses and more easily anticipated than others.

This study presents a first step in documenting a pathway to tropical cyclogenesis through vorticity accretion that may be applicable to other cases in the Caribbean basin. Sandy's cyclogenesis sequence as outlined herein should prove beneficial to hurricane forecasters, as it illustrates the potential positive impact an opening in the wave pouch can have on tropical cyclogenesis when the opening is superimposed on a favorable background environment.

7. Figures and tables

a. Figures

Acknowledgments.

The first two authors acknowledge the support from the National Research Council (NRC), through its Research Associateship Program, and the host institution, the Naval Postgraduate School (NPS) in Monterey, California. ECMWF data provided by Gerard Kilroy and Roger Smith from the Ludwig Maximilian University of Munich and the Deutscher Wetterdienst. CIMMS TPW data courtesy of Chris Velden. The work of all authors was partially supported by NASA grants NNH09AK561, NNG11PK021 and NNG09HG031 and by the National Science Foundation NSF AGS-0733380 and NSF AGS-0849356. Tim Dunkerton acknowledges NSF ATM-0851554.

REFERENCES

Blake, E. S., T. B. Kimberlain, R. J. Berg, G. P. Cangialosi, and J. L. Beven II, 2013: NHC tropical cyclone report 2012. Tech. rep., http://www.nhc.noaa.gov/2012atlan.shtml.

Charney, J. G. and A. Eliassen, 1964: On the growth of the hurricane depression. *J. Atmos. Sci.*, **21**, 68–75.

Cheung, K. K. W. and R. L. Elsberry, 2002: Tropical cyclone formations over the western north pacific in the navy operational global atmospheric prediction system forecasts. *Wea. Forecasting*, **17**, 800–820.

Dunkerton, T. J., M. T. Montgomery, and Z. Wang, 2009: Tropical cyclogenesis in a tropical wave critical layer: easterly waves. *Atmos. Chem. Phys.*, **9**, 5587–5646.

Gray, W. M. and R. W. Jacobson Jr., 1977: Diurnal variation of deep cumulus convection. *Mon. Wea. Rev.*, **105**, 1171–1188.

Harr, P. A., R. L. Elsberry, and J. C. Chan, 1996: Transformation of a large monsoon depression to a tropical storm during TCM-93. *Mon. Wea. Rev*, **124**, 2625–2643.

Haynes, P. H. and M. E. McIntyre, 1987: On the evolution of vorticity and potential vorticity in the presence of diabatic heating and frictional or other forces. *J. Atmos. Sci.*, **44**, 828–841.

Holland, G. J., 1983: Angular momentum transports in tropical cyclones. *Q. J. Roy. Meteor. Soc.*, **109**, 187–209.

Holton, J. R., 2004: *An Introduction to Dynamic Meteorology*. Academic press, Burlington, MA.

Ide, K., D. Small, and S. Wiggins, 2002: Distinguished hyperbolic trajectories in time-dependent fluid flows: analytical and computational approach for velocity fields defined as data sets. *Nonlinear Processes in Geophysics*, **9**, 237–263.

Killworth, P. D. and M. E. McIntyre, 1985: Do rossby-wave critical layers absorb, reflect, or over-reflect? *Journal of Fluid Mechanics*, **161**, 449–492.

Kilroy, G. and R. K. Smith, 2012: A numerical study of rotating convection during tropical cyclogenesis. *Q. J. Roy. Meteor. Soc.*

Landsea, C. W., 1993: A climatology of intense (or major) atlantic hurricanes. *Mon. Wea. Rev*, **121**, 1703–1713.

Malhotra, N. and S. Wiggins, 1998: Geometric structures, lobe dynamics, and lagrangian transport in flows with aperiodic time-dependence, with applications to rossby wave flow. *J. Nonlinear Sci.*, **8**, 401–456.

Mancho, A. M., D. Small, S. Wiggins, and K. Ide, 2003: Computation of stable and unstable manifolds of hyperbolic trajectories in two-dimensional, aperiodically time-dependent vector fields. *Physica D: Nonlinear Phenomena*, **182**, 188–222.

Montgomery, M. T., L. L. Lussier III, R. W. Moore, and Z. Wang, 2010a: The genesis of

Typhoon Nuri as observed during the Tropical Cyclone Structure 2008 (TCS-08) field experiment–Part 1: The role of the easterly wave critical layer. *Atmos. Chem. Phys.*, **10**, 9879–9900.

Montgomery, M. T. and R. K. Smith, 2014: Paradigms for tropical cylcone intensification. *Australian Meteor. Oceanogr. J.*, In Press.

Montgomery, M. T., Z. Wang, and T. J. Dunkerton, 2010b: Coarse, intermediate and high resolution numerical simulations of the transition of a tropical wave critical layer to a tropical storm. *Atmos. Chem. Phys*, **10**, 803–10.

Montgomery, M. T., et al., 2012: The Pre-Depression Investigation of Cloud-systems in the Tropics (PREDICT) experiment. *Bull. Am. Meteor. Soc.*, **93**, 153–172.

NASA, 2013: HS3 hurricane mission. URL `http://www.nasa.gov/mission_pages/hurricanes/missions/hs3/overview/`, URL `http://www.nasa.gov/mission_pages/hurricanes/missions/hs3/overview/`.

Okubo, A., 1970: Horizontal dispersion of floatable particles in the vicinity of velocity singularities such as convergences. *Deep Sea Research and Oceanographic Abstracts*, Elsevier, Vol. 17, 445–454.

Riemer, M. and M. T. Montgomery, 2011: Simple kinematic models for the environmental interaction of tropical cyclones in vertical wind shear. *Atmos. Chem. Phys*, **11**, 9395–9414.

Rutherford, B. and M. T. Montgomery, 2012: A Lagrangian analysis of a developing and non-developing disturbance observed during the PREDICT experiment. *Atmos. Chem. Phys.*, **12**, 11 355–11 381.

Schecter, D. A. and M. T. Montgomery, 2006: Conditions that inhibit the spontaneous radiation of spiral inertia-gravity waves from an intense mesoscale cyclone. *J. Atmos. Sci.*, **63**, 435–456.

Shen, B.-W., M. DeMaria, J.-L. Li, and S. Cheung, 2013: Genesis of hurricane sandy (2012) simulated with a global mesoscale model. *Geophysical Research Letters*, **40 (18)**, 4944–4950.

Smith, R. K., M. T. Montgomery, and N. Van Sang, 2009: Tropical cyclone spin-up revisited. *Q. J. Roy. Meteor. Soc.*, **135**, 1321–1335.

Wang, Z., M. T. Montgomery, and T. J. Dunkerton, 2009: A dynamically-based method for forecasting tropical cyclogenesis location in the atlantic sector using global model products. *Geophys. Res. Lett.*, **36**.

Wang, Z., M. T. Montgomery, and T. J. Dunkerton, 2010a: Genesis of pre–hurricane Felix (2007) Part I: The role of the easterly wave critical layer. *J. Atmos. Sci.*, **67**, 1711–1729.

Wang, Z., M. T. Montgomery, and T. J. Dunkerton, 2010b: Genesis of pre–hurricane Felix (2007) Part I: Warm core formation, precipitation evolution and predictability. *J. Atmos. Sci.*, **67**, 1730–1744.

Weiss, J., 1991: The dynamics of enstrophy transfer in two-dimensional hydrodynamics. *Physica D: Nonlinear Phenomena*, **48**, 273–294.

Wiggins, S. and J. Guckenheimer, 1992: Chaotic transport in dynamical systems. *Physics Today*, **45**, 68.

Willoughby, H. E., 1990: Gradient balance in tropical cyclones. *J. Atmos. Sci.*, **47**, 265–274.

List of Figures

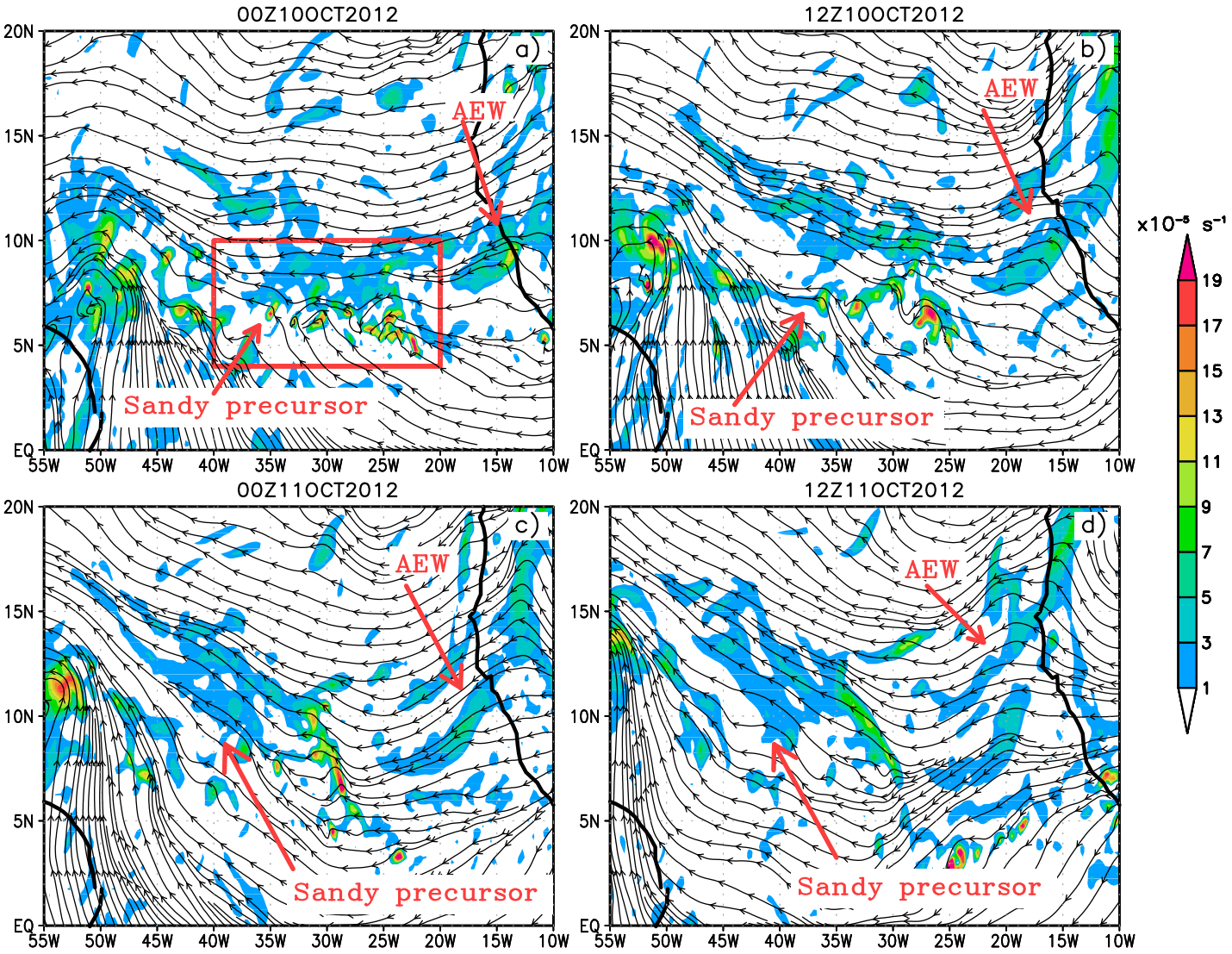

Figure 1: Four-panel plot of 700 hPa ECMWF streamlines (earth-relative) and relative vorticity (shaded) valid at 12-h intervals from 10-11 Oct. The red box in the first panel indicates the region of the ITCZ breakdown and the red arrows highlight the AEW.

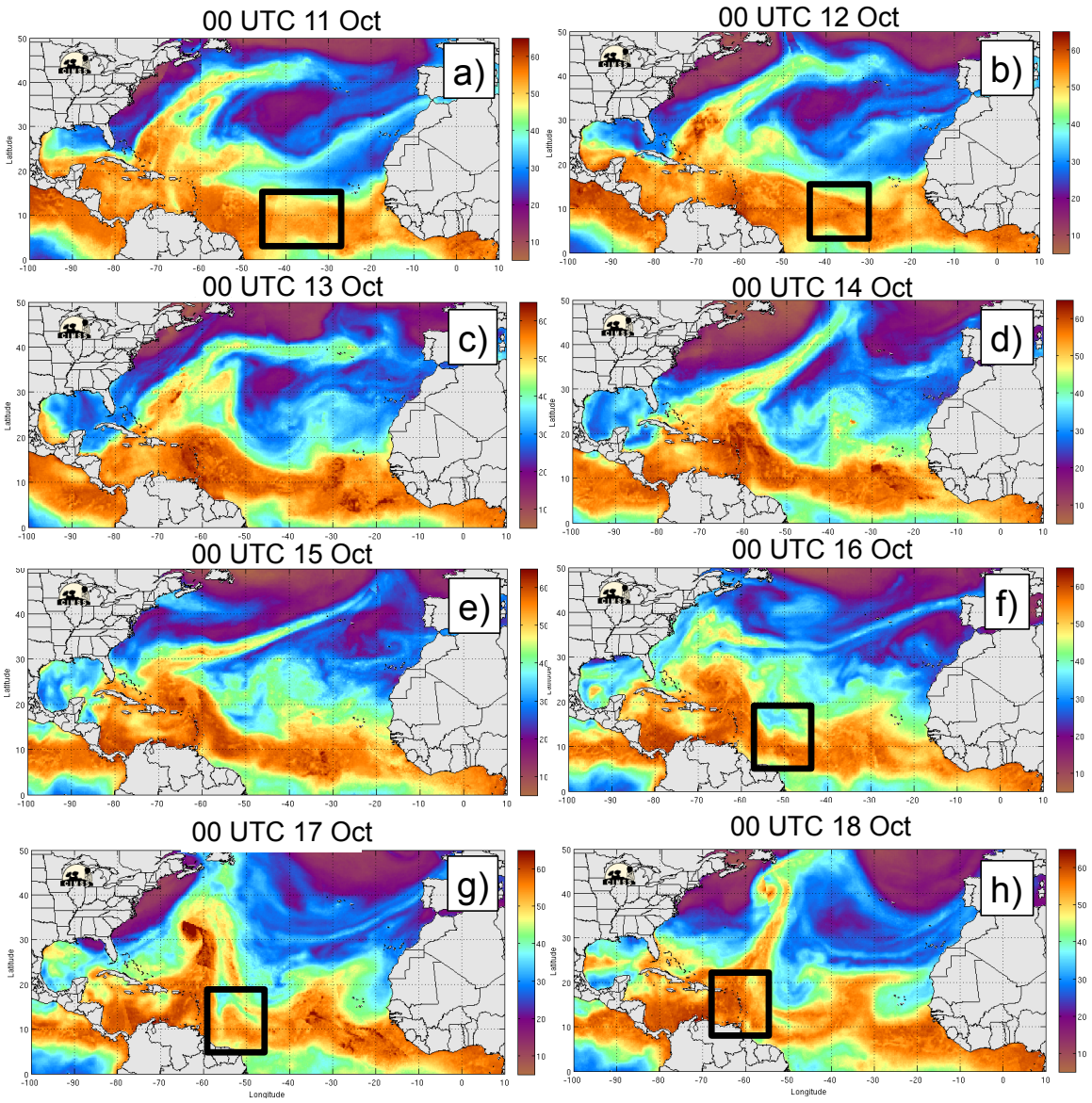

Figure 2: Eight-panel plot of CIMMS TPW valid at 00 UTC from 11-18 Oct. The black box highlights the location of the pre-Sandy wave when it is identifiable in the analysis.

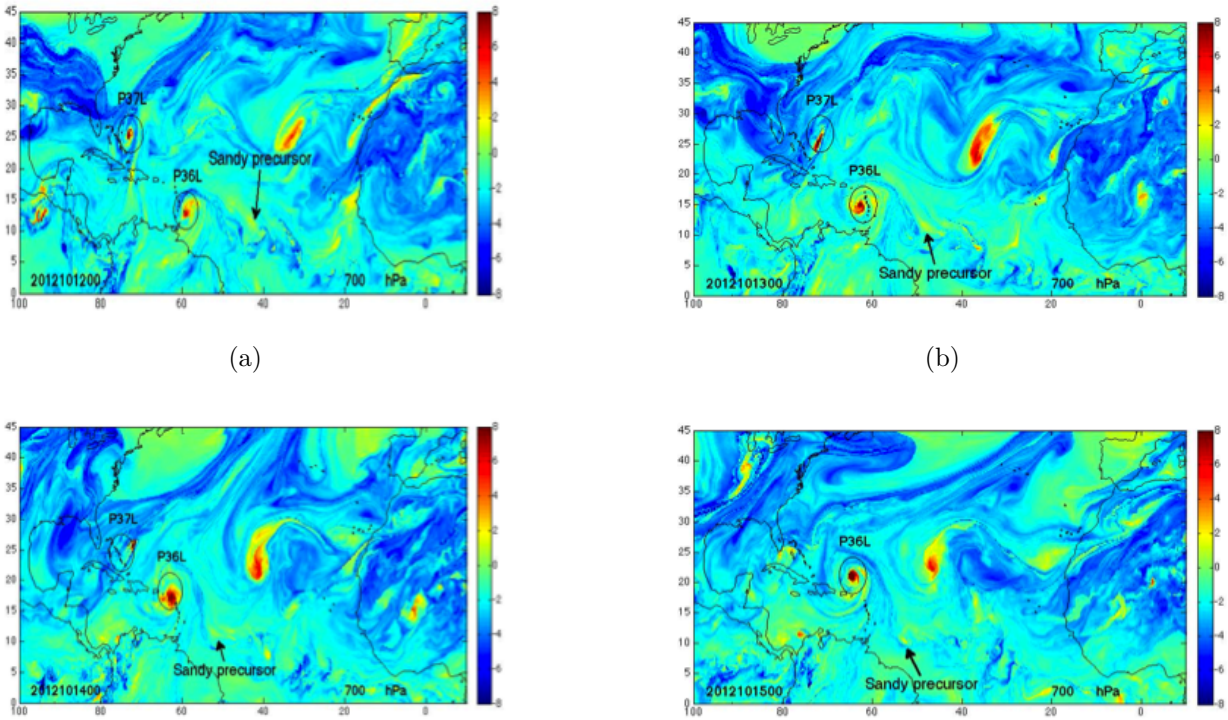

Figure 3: The Lagrangian OW fields show the pre-Sandy wave as a region of enhanced rotation at 00 UTC 12-15 Oct. The black circles indicate other storms being tracked during this time period: Hurricane Raphael (P36L) and Tropical Storm Patty (P37L).

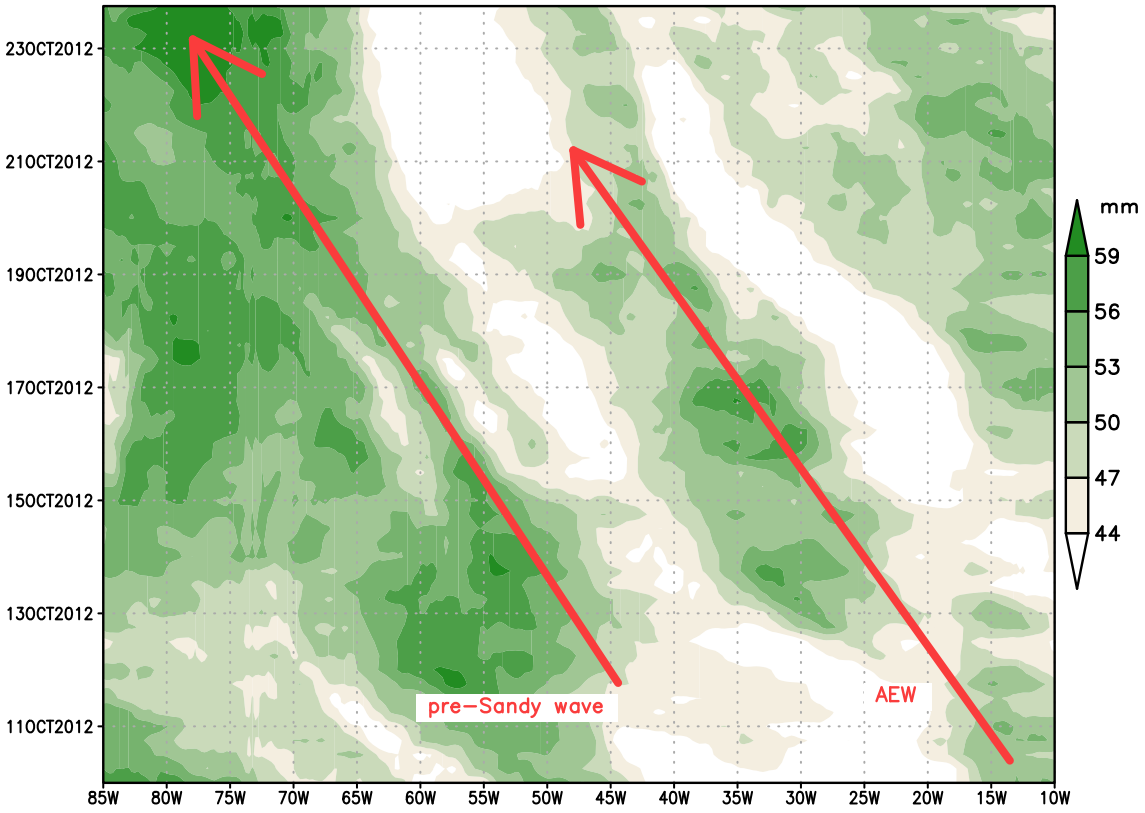

Figure 4: Hovmoeller diagram of ECMWF-derived TPW latitudinally-averaged between 10-14 N for the period of 00 UTC 10 Oct1–18 UTC 23 Oct.

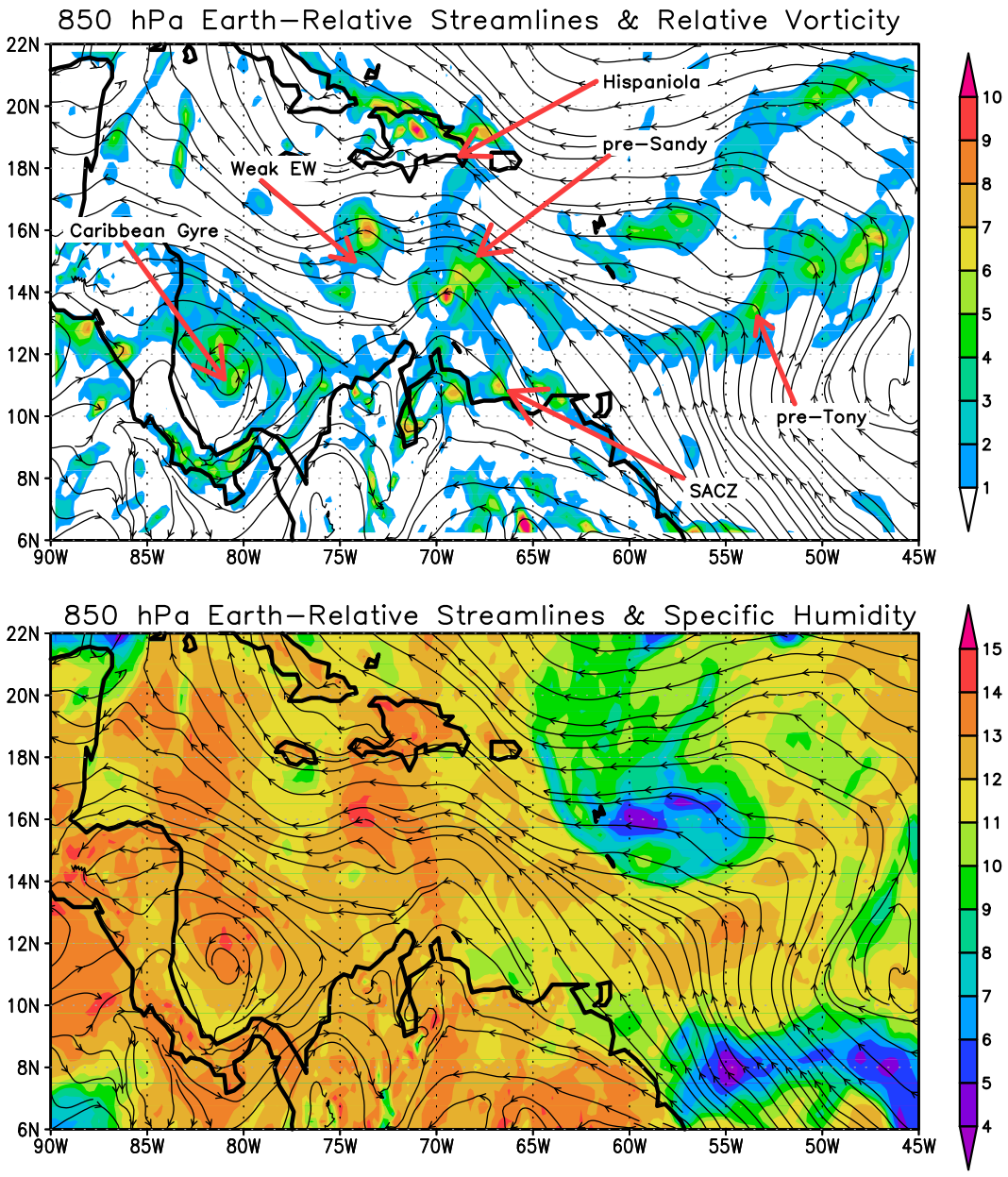

Figure 5: Analysis from the ECMWF at 850 hPa valid at 18 UTC 19 Oct. The top panel is relative vorticity ($x10^{-5}s^{-1}$) and the bottom is specific humidity ($g\,kg^{-1}$). Both panels are overlaid with streamlines in the earth-relative frame.

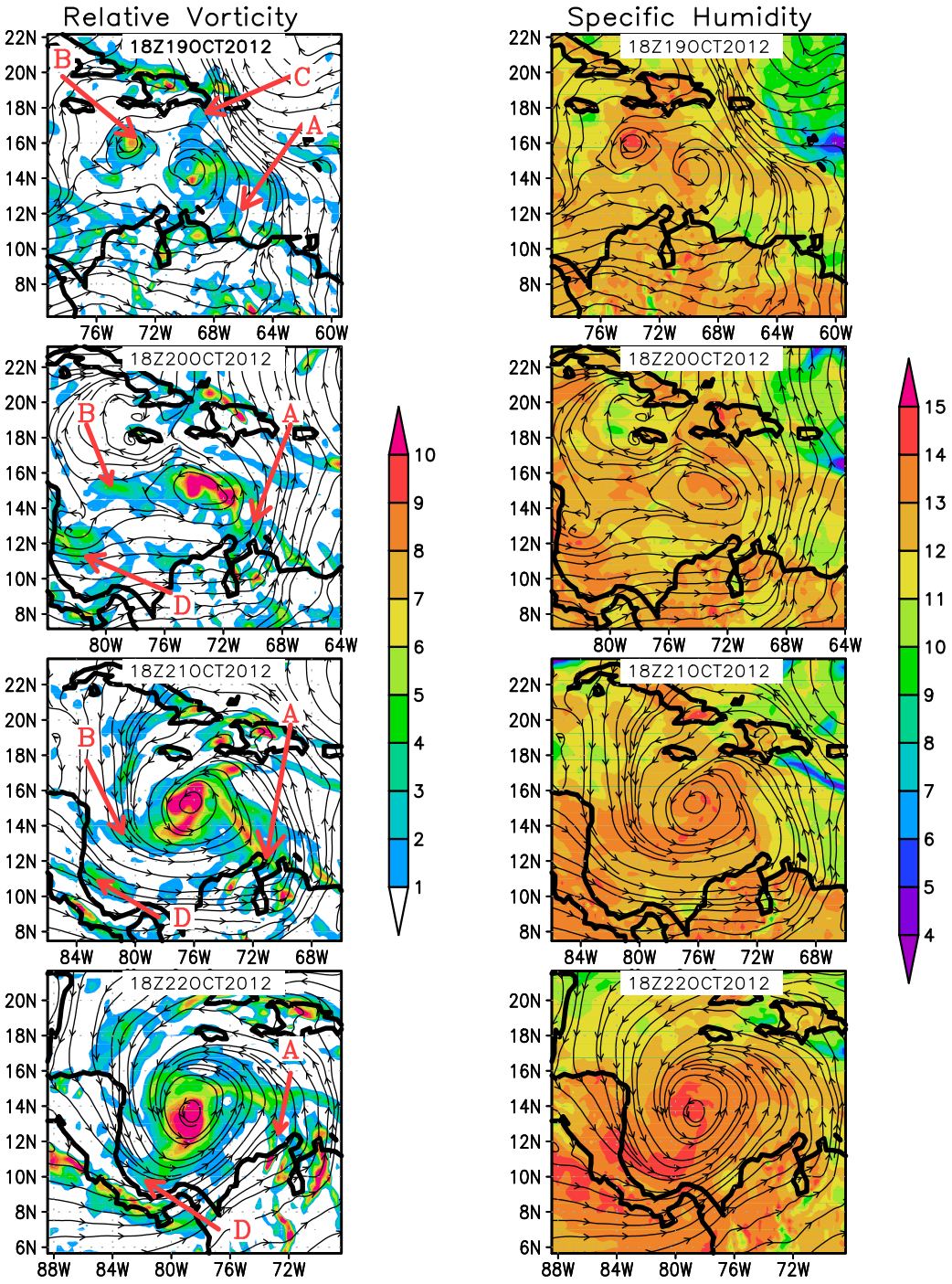

Figure 6: Analysis from the ECMWF at 850 hPa ECMWF valid at 24-h intervals from 18 UTC 19-22 Oct. The left panels depict relative vorticity ($x10^{-5}s^{-1}$) and the right panels depict specific humidity (gkg^{-1}). Both panels are overlaid with streamlines in the co-moving frame. The letters in the left panel represent areas of potential vorticity accretion discussed in the text: A) the SACZ; B) the weak EW; C) cyclonic vorticity generated along Hispaniola; and D) cyclonic vorticity potentially associated with the Caribbean Gyre.

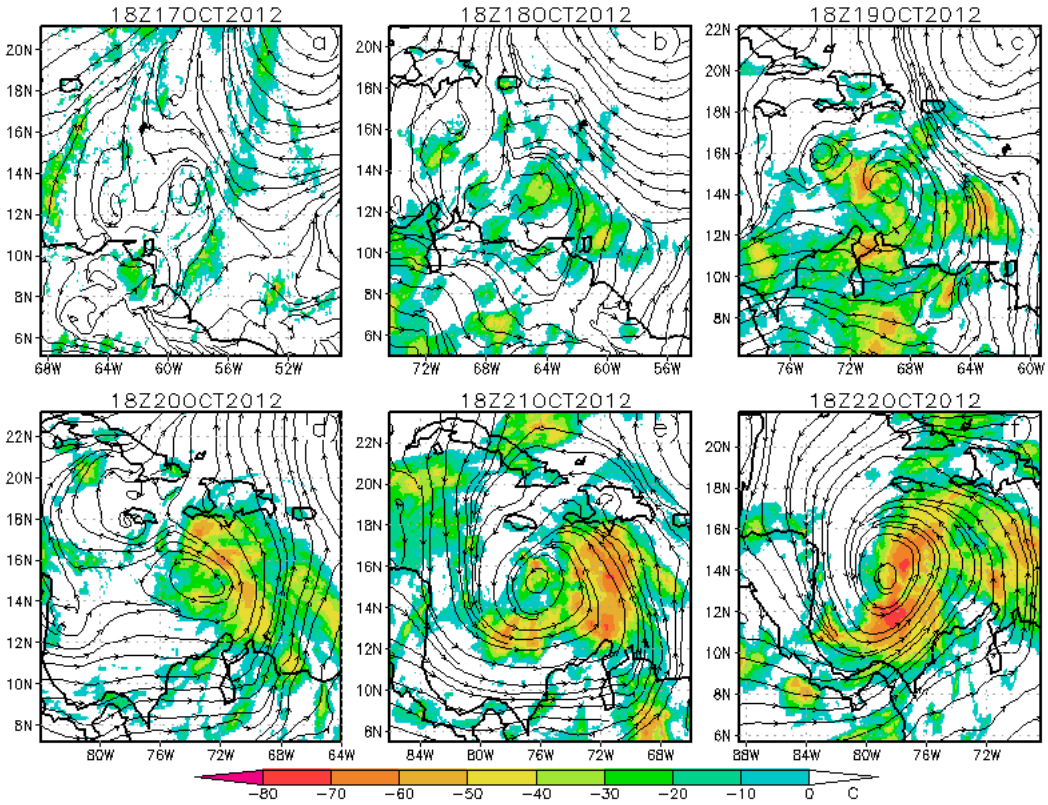

Figure 7: Six-hour mean IR brightness temperature overlaid on 850 hPa ECMWF analysis co-moving streamlines at 24-h intervals (17-22 Oct). The time averaging is centered on the valid time of each figure.

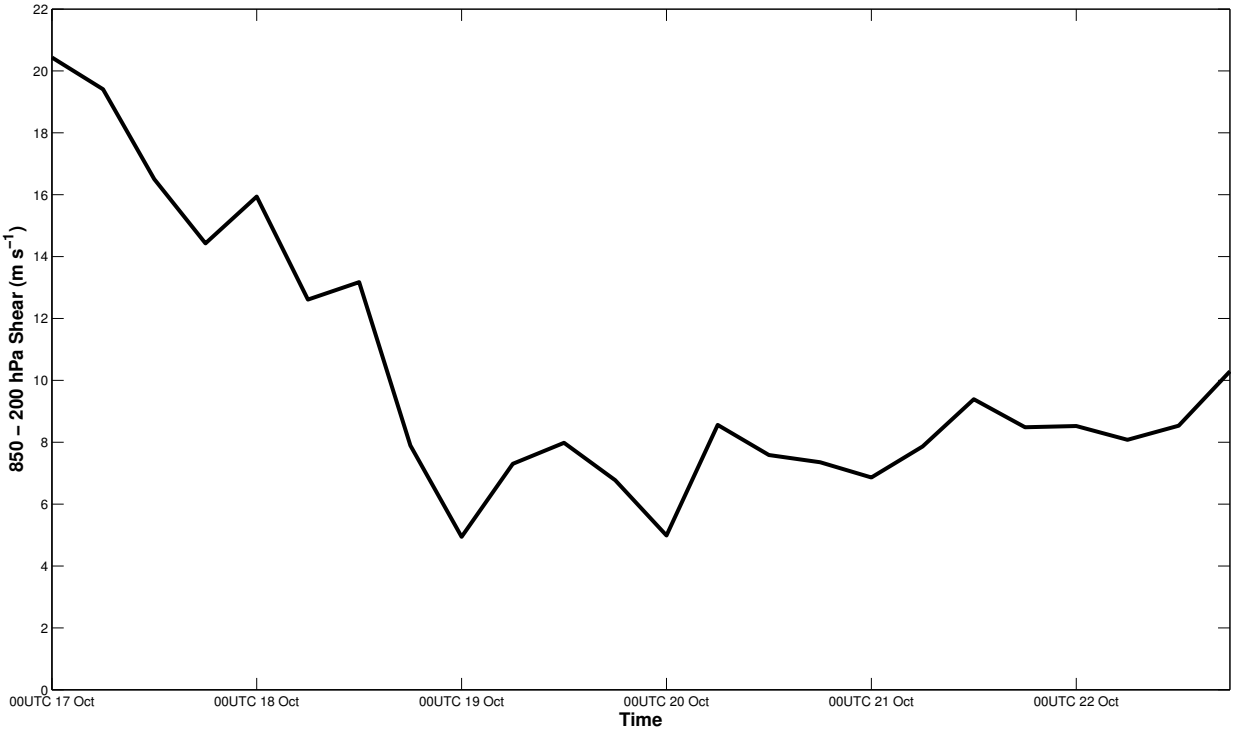

Figure 8: Time evloution of 850-200 hPa shear from the ECMWF analysis valid at six hour intervals beginning at 00UTC 17 Oct. The time series displays the average shear vector magnitude within 3° x 3° box centered on and moving with the sweet spot position.

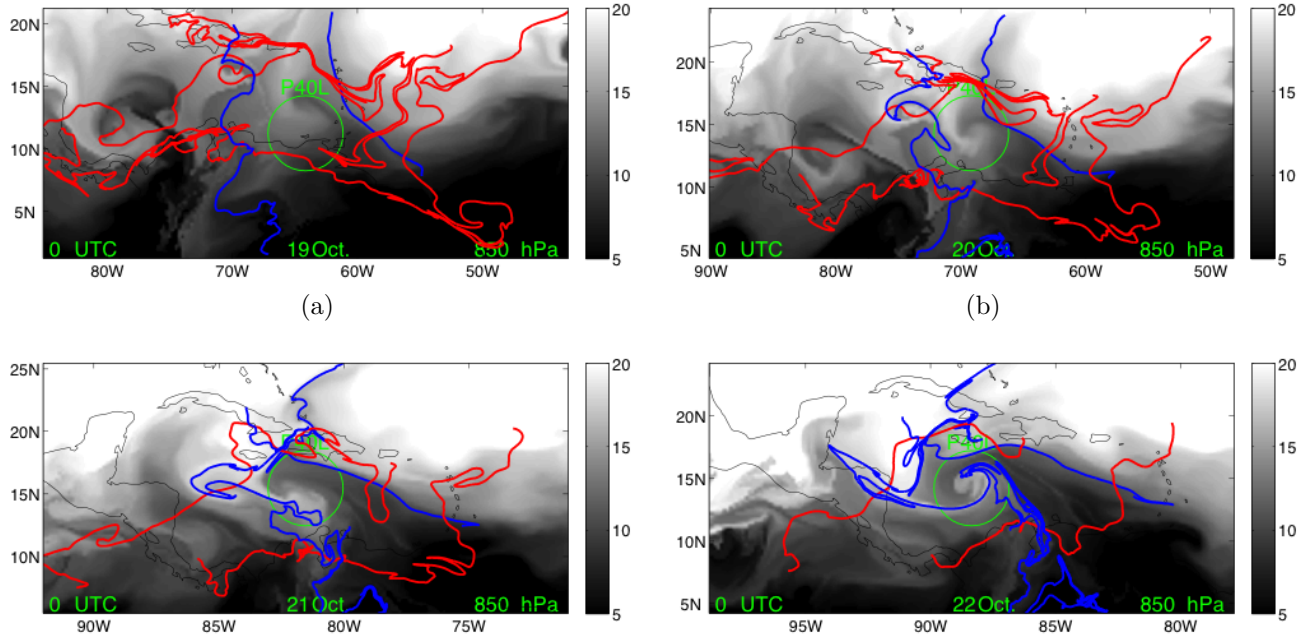

Figure 9: The stable (red) and unstable (blue) manifolds are shown at the 00 hour analysis times and overlaid on the latitude tracer field at the same times from 19-22 Oct. The manifolds are computed in the time interval ranging from 18 Oct when the saddle points emerge and the unstable manifold is initialized, to 23 Oct when the western saddle point vanishes and the stable manifold is initialized. The latitude tracer field displays the latitude of air parcels 48 hours prior to their shown locations.

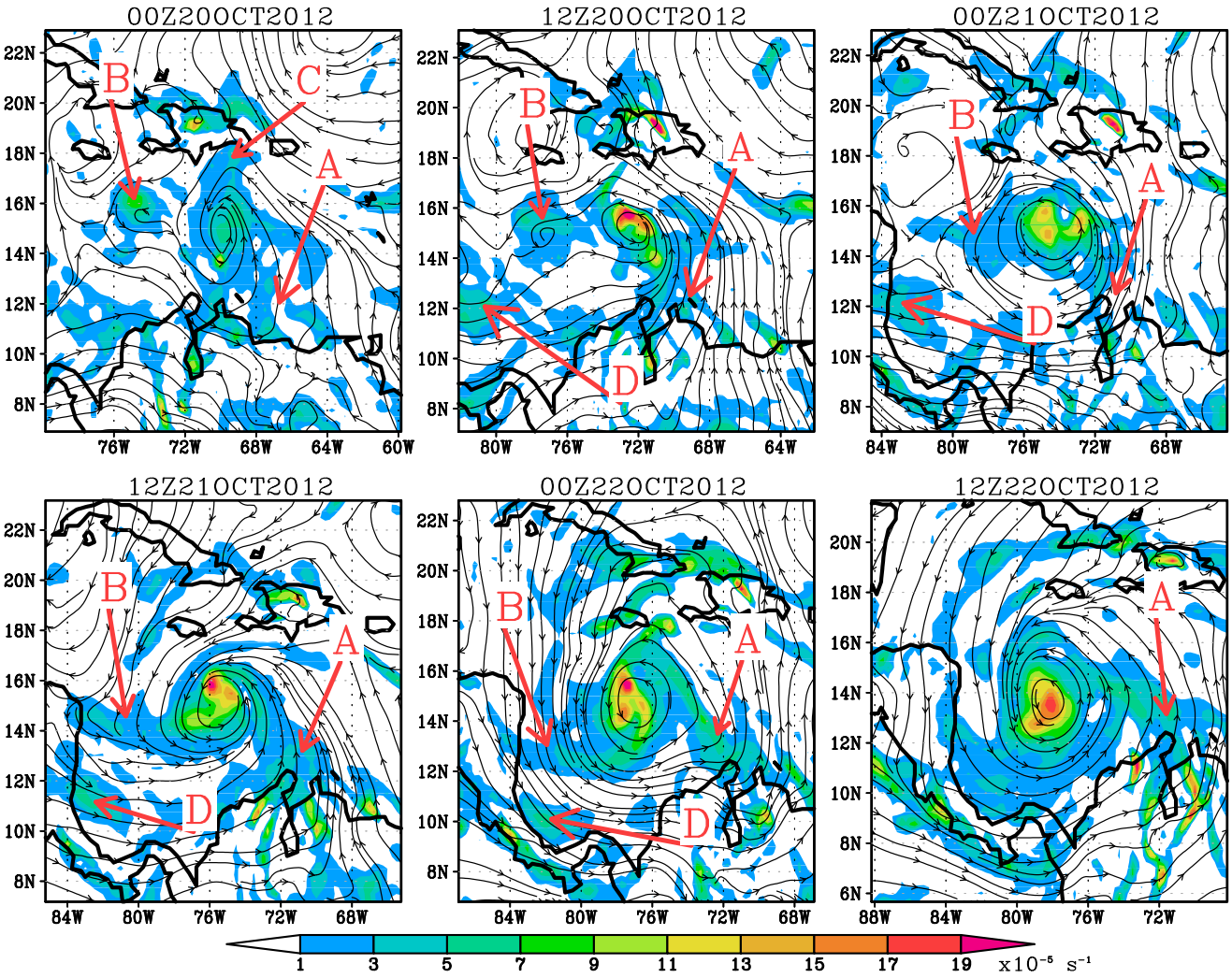

Figure 10: Six-panel plot of co-moving streamlines and relative vorticity at 850 hPa valid at 12-hr intervals from the ECMWF analysis. The letters and arrows highlight potential candidates for accretion of vorticity into the pre-Sandy pouch including: A) The SACZ, B) the weak EW, C) cyclonic vorticity generated south of Hispaniola, and D) cyclonic vorticity filaments near 81W.

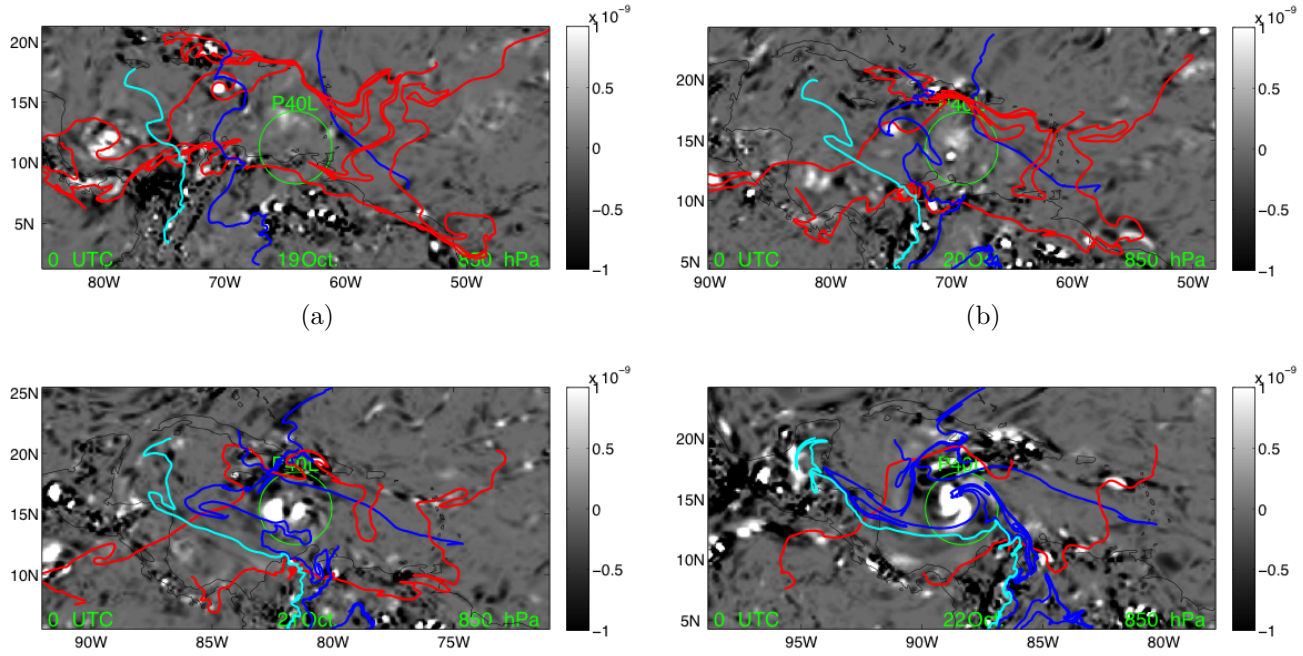

Figure 11: Stable (red) and unstable (blue) Lagrangian manifolds overlaid on the relative vorticity field from the 850 hPa ECMWF analysis valid at 00 UTC each day from 19-22 Oct.

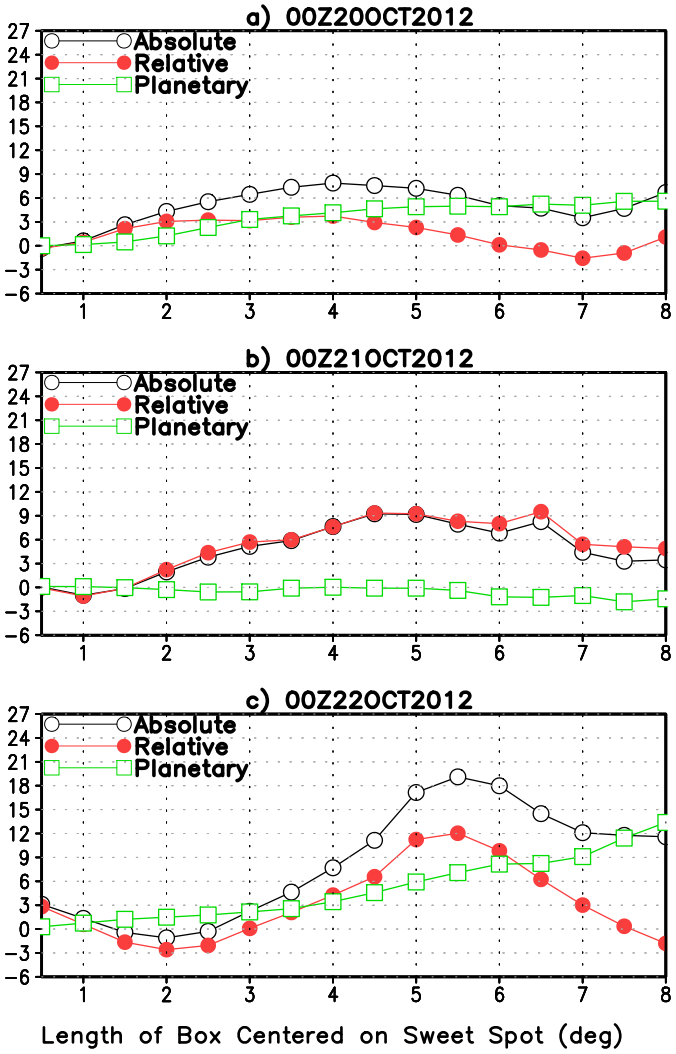

Figure 12: Three-panel plot of 850 hPa absolute (black), relative (red), and planetary (green) advective vorticity flux convergence ($km^2 s^{-1} dy^{-1}$) from the ECMWF analysis data. The flux is calculated as in Eq. (6) through 0.5 degree length boxes centered on and moving with the sweet spot position. These data are temporally-averaged, from 18 UTC the previous day to 00 UTC of the indicated day. The plots are valid every 24 hours beginning at 00 UTC 20 Oct.

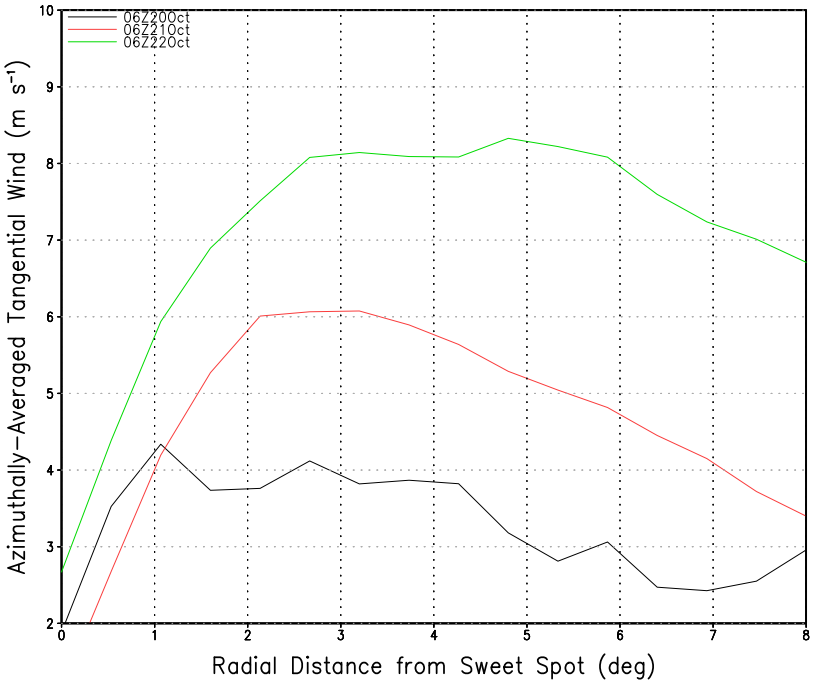

Figure 13: Azimuthally-averaged 850 hPa tangential wind profiles plotted by radial distance from the sweet spot position derived from the ECMWF analysis for 20-22 Oct.

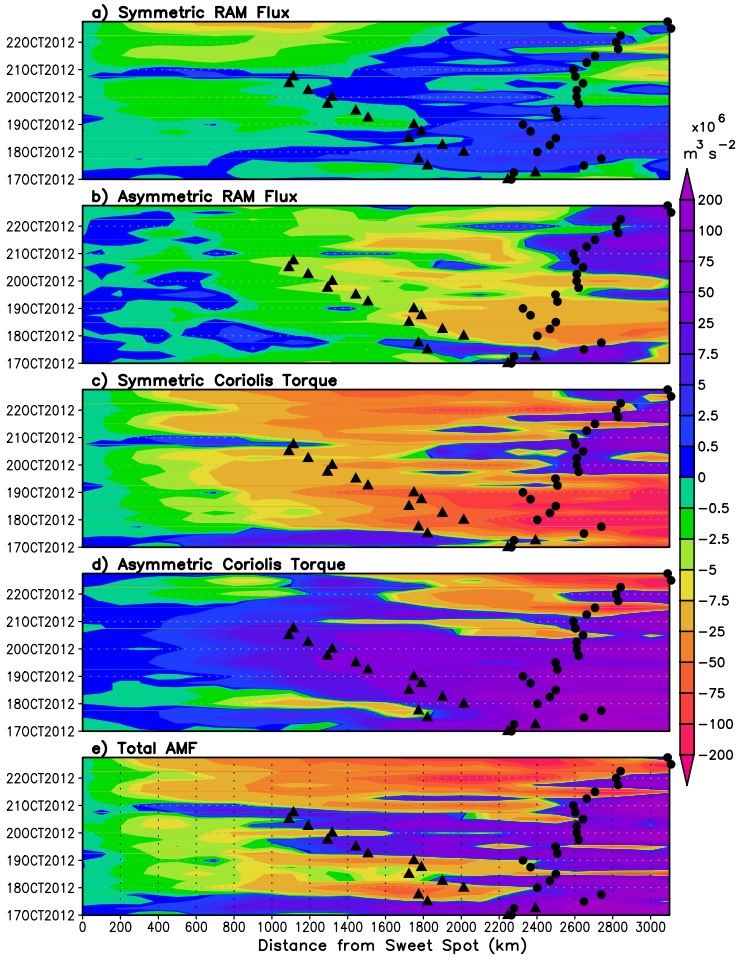

Figure 14: Hovmoeller diagrams derived from the ECMWF analysis of each term of the angular momentum flux equation at 850 hPa. The terms are calculated in radial distances from the sweet spot position. The black circles are the approximate distance of the center of the pre-Tony disturbance and the triangles are the approximate position of the Caribbean Gyre center. The abscissa is radial distance (km) and the ordinate is time.

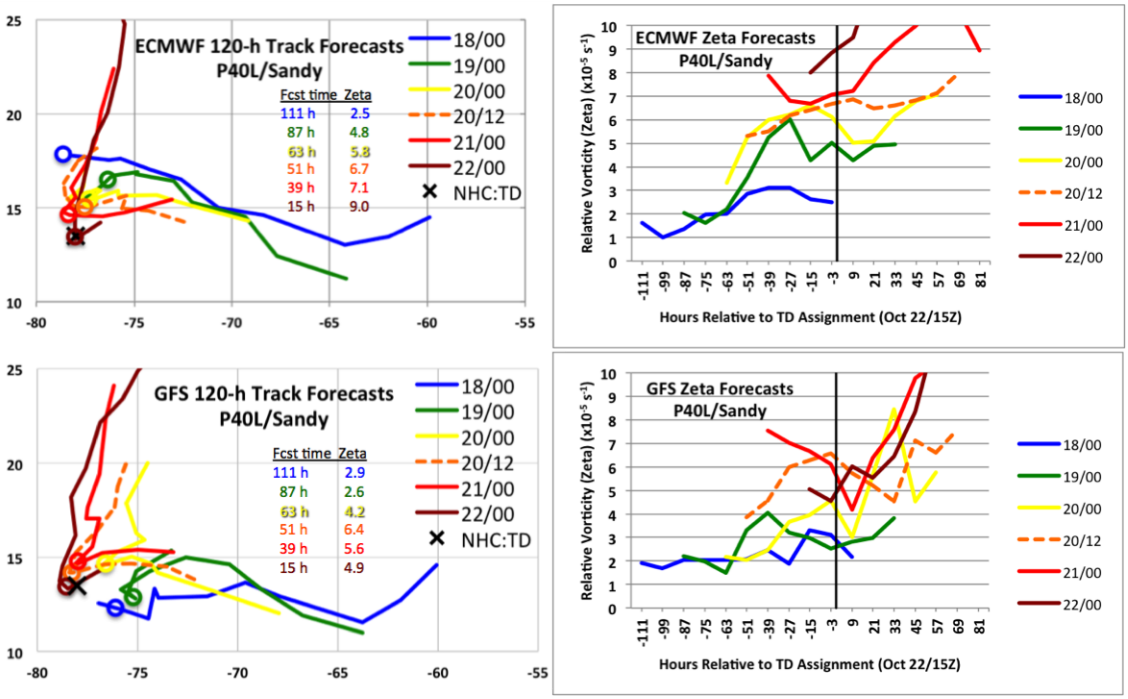

Figure 15: Position (left) and intensity (right) forecasts for Hurricane Sandy from the ECMWF (top) and GFS (bottom) global forecast models. Each colored line corresponds to an initial forecast time (as per the insert). The circles on the position figures indicate the time of NHC TD declaration. For the position forecasts, the abscissa is longitude and the ordinate is latitude. For the intensity forecasts, the zero hour on the abscissa is the time NHC declared the storm a TD and is indicated by the thick vertical line.